Received: 24 June 2019 | Revised: 23 July 2019 | Accepted: 25 July 2019

DOI: 10.1002/er.4808

RESEARCH ARTICLE

WILEY INTERNATIONAL JOURNAL OF ENERGY RESEARCH

Experimental and optimization studies of hydrogen production by steam methane reforming over lanthanum strontium cobalt ferrite supported Ni catalyst

Bamidele Victor Ayodele[1,2] | **Siti Indati Mustapa**[1] | **Mohamed Yazrul Bin Mohd Yassin**[2,3] | **Sureena Abdullah**[2,3]

[1] Institute of Energy Policy and Research, Universiti Tenaga Nasional, Jalan IKRAM-UNITEN, 43000 Kajang, Selangor, Malaysia

[2] Center of Excellence for Advanced Research in Fluid Flow, Lebuhraya Tun Razak, 26300Gambang, Pahang, Malaysia

[3] Faculty of Chemical and Natural Resources Engineering, Universiti Malaysia Pahang, Lebuhraya Tun Razak, 26300Gambang, Pahang, Malaysia

Correspondence
Bamidele Victor Ayodele and Sureena Abdullah, Center of Excellence for Advanced Research in Fluid Flow Lebuhraya Tun Razak, 26300 Gambang Kuantan, Pahang, Malaysia.
Email: sureena@ump.edu.my, ayodelebv@gmail.com

Funding information
Universiti Malaysia Pahang, Grant/Award Number: RDU150397

Summary

Over the years, research focused has been on the development of active and stable catalysts for hydrogen (H_2) production by steam methane reforming (SMR). However, there is less attention on the individual and interaction effect of key process parameters that influence the catalytic performance of such catalysts and how to optimize them. The main objective of this study is to investigate the individual and interaction effects of key parameters such as methane partial pressure (P_{CH_4}) (10-30 kPa), steam partial pressure ($P_{H_2O(g)}$) (10-30 kPa), and reaction temperature (T) (750-850°C) on H_2 yield and methane (CH_4) conversion during SMR using Box-Behnken experimental design (BBD) and response surface methodology. The H_2 production was catalyzed using Ni/LSCF prepared by wet impregnation method. The evaluation of the Ni/LSCF using different instrument techniques revealed that the catalyst exhibited excellent physicochemical properties suitable for SMR. Response surface models showing the individual and interaction effect of each of the parameters on the H_2 yield and CH_4 conversion were obtained using the set of data obtained from the BBD matrix. The three parameters were found to have significant effects on the H_2 yield and CH_4 conversion. At the highest desirability of 0.8994, maximum H_2 yield and CH_4 conversion of 89.77% and 89.01%, respectively, were obtained at optimum conditions of 30 kPa, 28.86 kPa, and 850°C for P_{CH_4}, $P_{H_2O(g)}$, and temperature, respectively. The predicted values of the responses from the response surface models were found to be in good agreement with the experimental values. At optimum conditions, the catalyst was found to be stable up to 390 minutes with time on stream. The characterization of the used catalyst using thermogravimetric analysis, scanning electron microscopy, energy-dispersive X-ray spectroscopy, and transmission electron microscopy showed some evidence deposition of a small amount of carbon on the catalyst surface.

KEYWORDS

Box-Behnken design, desirability function, lanthanum strontium cobalt ferrite, response surface methodology, steam methane reforming

 © 2019 John Wiley & Sons, Ltd.

1 | INTRODUCTION

For over a century, there has been a remarkable interest in H_2 production as an alternative and sustainable source of energy..[1] This is due to its numerous merits as a source of energy over the conventional fossil fuel.[2] Hydrogen as a fuel has been reported to have zero-emission when combusted in the presence of oxygen.[3] According to Dutta,[4] H_2 is a good energy carrier and possesses the highest energy density compared with other forms of fuels. Moreover, H_2 has been reported to have high energy yield (about 122 kJ/kg) making it better than fossil fuel.[5] Hydrogen finds wide applications in fuel cell technology,[6] internal combustion engines,[7] as feedstock for the production of gasoline,[4] methanol,[8] fertilizer,[9] and other valuable chemicals. Due to its importance and applications in industrial processes, H_2 has been adjudged as the energy of the future.[10] As a result of this, several technological routes such as coal and biomass gasification,[11] hydrocarbon reforming,[12] thermochemical water splitting,[13] photo-electrolysis,[14] and biomass pyrolysis[15] have been employed to achieve the possibility of producing H_2 in abundance and make it readily available. According to Parthasarathy and Narayanan,[16] the various feedstock used for the production of H_2 includes coal, natural gas, liquid hydrocarbons, and other alternative sources. Among these various feedstocks, natural gas accounts for 49% of total H_2 produced.[16]

Natural gas, which is abundant in nature, has been the main feedstock used for producing H_2 by steam methane reforming (SMR).[17] SMR is a matured technology used commercially for hydrogen production.[18] The SMR process is an endothermic reaction, which entails the oxidation of methane (CH_4) by steam in the presence of a catalyst to produce H_2, carbon monoxide (CO), and little amount of carbon dioxide (CO_2) as shown in the sequential reactions below.[19]

$$CH_4 + H_2O\ (\text{steam}) \leftrightarrow CO + 3H_2$$

$$H^{o}_{25oC} = 206.2\ \text{kJ/mol}$$

$$CO + H_2O\ (\text{steam}) \leftrightarrow CO_2 + H_2$$

$$H^{o}_{25oC} = 41.1\ \text{kJ/mol}$$

$$CH_4 + 2H_2O\ (\text{steam}) \leftrightarrow CO_2 + 4H_2$$

$$H^{o}_{25oC} = 165\ \text{kJ/mol}$$

where $H^{o}_{25\ oC}$ is the standard enthalpy change at 25°C.

The SMR is highly temperature-dependent that occurs at a temperature range of 800 to 1000°C over Nickel catalysts.[20] Hence, catalyst deactivation has been the major challenges that have been confronting the SMR process.[21] An comprehensive review by Iulianelli et al[22] revealed that several catalysts have been developed and utilized for SMR to produce H_2.[19] These catalysts are mainly supported Ni catalysts, and few noble metals such as Ru, Rh, Pd, Pt, and Ir.[19,23-25] However, nickel-based catalysts accounted for over 60% of the total publication outputs on SMR due to high activity towards H_2 production as well as their low cost compared with noble metals.[25] Nevertheless, nickel-catalysts are susceptible to deactivation by sintering and carbon deposition.[19,26] To overcome these constraints, several researchers have adopted techniques such as using suitable supports[27] and promoters[28] as well as optimizing the process parameters to reduce coke formation.[29] Till now, supports such as Al_2O_3, CeO_2, La_2O_3, ZrO_2, SiO_2, SBA-15, and perovskite $LaFeO_3$ have been used for the synthesis of Ni catalysts employed for SMR.[28,29] These supports were reported to have a varying degree of influence on the stability and the activities of the nickel catalysts during SMR reaction.[30] Recently, Yang et al[31] in their extensive review reiterate the importance of using perovskite-type oxides as precursors for preparing supported metal catalyst. Lian et al[30] employed perovskite $LaFeO_3$ as support for Ni catalyst used in SMR to H_2. The findings revealed that there was improved Ni dispersion on the perovskite $LaFeO_3$. Moreover, the catalyst displayed high thermal stability and catalytic activity for H_2 production. LSCF has been extensively used as a catalyst in solid oxide fuel cells (SOFCs) but not as catalyst support. In our previous study, the catalytic performance of LSCF and Al_2O_3-supported Ni catalyst was compared in SMR to H_2. The study revealed that Ni/LSCF catalyst has superior activity compared with Ni/Al_2O_3 catalyst. However, the catalyst was observed to deactivate after 300 minutes of time-on-stream. Studies have shown that the combinations of appropriate parameters can improve catalysis activity and stability.[32] Raheem et al[32] employed central composite design and responsible surface methodology to investigate the effect of reaction temperature, catalyst loading, and reaction time on H_2-rich syngas production by catalytic gasification of algal. The H_2-rich syngas production was reported to be significantly influenced by reaction temperature and time. Maximum H_2 yield of 48.98% was obtained at optimum conditions of 850°C, 16.4wt% catalyst loading, and reaction time of 28.8 minutes. In a similar study, Patcharavorachot et al[33] in their optimization studies reported that reaction temperature, pressure, and steam to glycerol ratio had significant effects on H_2 production by glycerol reforming. The effects of Ce and Ni loading on the yield of H_2 during catalytic propane reforming have been investigated by Azizzadeh Fard et al.[34] Maximum H_2 yield of 63% was obtained at optimum conditions of 11.85 wt%Ni and 3.55 wt% Ce. Till date, there are scanty studies on experimental

design and optimization of H_2 production by SMR using response surface approach. To the best of the authors' knowledge, the interaction effects of key process parameters such as CH_4 partial pressure, steam partial pressure, and the reaction temperature on the rate of CO-rich H_2 production by SMR over Ni/LSCF catalyst has not been investigated. Therefore, this study aimed to investigate the interaction of key process parameters (P_{CH_4}, $P_{H_2O(g)}$, and T) on the H_2 production using Box-Behken experimental design and response surface technique. Moreover, the optimum conditions of these parameters that maximize the activity and enhance the stability of the Ni/LSCF catalyst during SMR to H_2 were also investigated. The choice of response surface approach employed in these studies is due to its flexibility and robustnes as an optimization tool that has been extensively used in various process optimization.[35] The interaction effects of the process parameters on the process response can be thoroughly explained and clarify using response surface technique.[34]

2 | EXPERIMENTAL

2.1 | Catalyst preparation

The steps and the detail description involved in the preparation of the Ni/LSCF catalyst has been reported in Ayodele et al[36] and summarized in Figure 1.

As shown in Figure 1, the stages involve in the preparation of the Ni/LSCF catalyst include the preparation of the aqueous Ni $(NO_3)_2.6H_2O$, impregnation of the aqueous Ni $(NO_3)_2.6H_2O$ into the LSCF, mixing of the aqueous Ni $(NO_3)_2.6H_2O$ and LSCF slurry at room temperature for 3 hours, drying in the oven at 105°C for 2 hours, calcination at 900°C for 6 hours at the rate of 10°C/min, and in situ reduction at 900°C for 2 hours at the rate of 10°C/min. Typically, the catalyst was prepared by calculating the amount of Ni $(NO_3)_2.6H_2O$ equivalent to 5wt% Ni loading and dissolved in di-ionized water to form an aqueous solution of Ni $(NO_3)_2.6H_2O$. The Ni $(NO_3)_2.6H_2O$ (aq) was subsequently impregnated into the LSCF under continuous stirring at 25°C for 3 hours. Thereafter, the slurry formed was oven-dried for at 105°C for 24 hours and afterward calcined at 900°C for 6 hours at a heating rate of 10°C/min. Prior to the commencement of the experimental runs for the optimization study, the catalyst was reduced in situ at 900°C for 2 hours.

2.2 | Determination of the physicochemical properties of the catalyst

The detail description and steps involved in the determination of the physicochemical properties of the fresh and used Ni/LSCF catalyst have been reported in Ayodele et al[36] and summarized in Figure 2. The physicochemical properties evaluated for the fresh Ni/LSCF catalysts include textural properties using the BET and BJH methods, the elemental composition, the crystallinity, surface morphology, reducibility, and microstructure, while the amount of carbon deposited on the used catalyst was quantified using thermogravimetric analysis (TGA). The X-ray diffraction (XRD) analysis was performed on PANALYTICAL X'PERT machine. The textural properties were investigated using Micrometrics ASAP 2020. The scanning electron microscopy (SEM) and energy-dispersive X-ray spectroscopy (EDX) analysis were carried out using Hitachi bench top (TM 3030 PLUS). TECNAL G2F20 TEM machine was employed for the transmission electron microscopy (TEM) analysis of the microstructure of the catalyst. The extent of reducibility was investigated using Thermo-Scientific 1100 fitted with a thermal conductivity detector (TCD). The amount of carbon deposited on the used Ni/LSCF catalysts was quantified using STA 7000 series thermogravimetric analyzer.

3 | BOX BEHNKEN EXPERIMENTAL DESIGN AND HYDROGEN OPTIMIZATION STUDIES

A three-factor three-level Box-Behnken experimental design (BBD) is employed in this study to perform the experimental design for the optimization studies and to also investigate the interaction between the parameters. BBD is a form of response surface design with the feature of an independent quadratic design or polynomial model (a design that does encompass an embedded factional or fractional factorial design) represented in the equation below.[37,38]

$$Y_i = \beta_o + \sum_{j=1}^{k}\beta_j x_j + \sum_{j=1}^{k}\beta_{jj} x_j^2 + \sum\sum_{j<1}^{k}\beta_{ij} x_i x_j,$$

where predicted responses, the offset term, the linear effect, the square effect, and the interaction effects are represented by Y_i, β_o, β_j, β_{jj}, and β_{ij}, respectively.

The BBD entails the placing of the treatment combinations at the midpoints of process space edges as well as the center.[39] The main advantage of the BBD is the fewer treatment combinations requirement compared with the central composite design.[40] The parameters (variable) investigated in this study include CH_4 partial pressure, steam partial pressure, and the reaction temperature, while the responses are CH_4 conversion and H_2 yield. The parameters were studied at two levels, namely, low level and high level (coded as −1 and +1, respectively).

LIST OF FIGURES

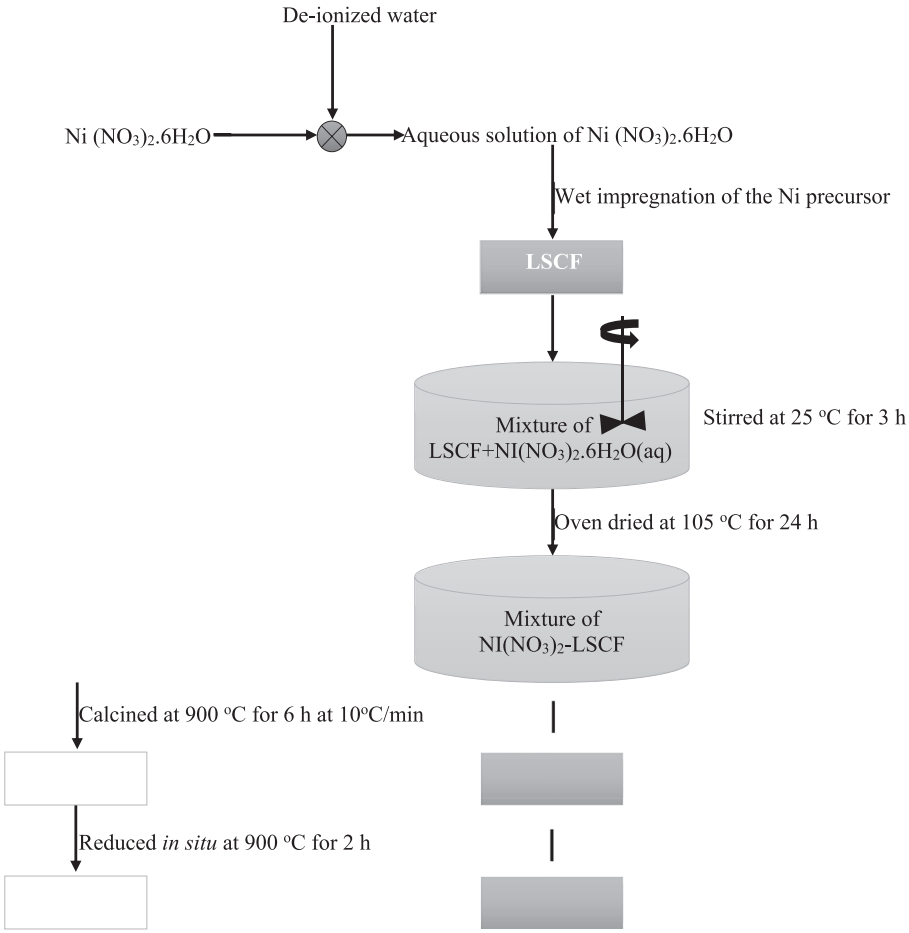

FIGURE 1 Stages involved in the preparation of the Ni/LSCF catalyst

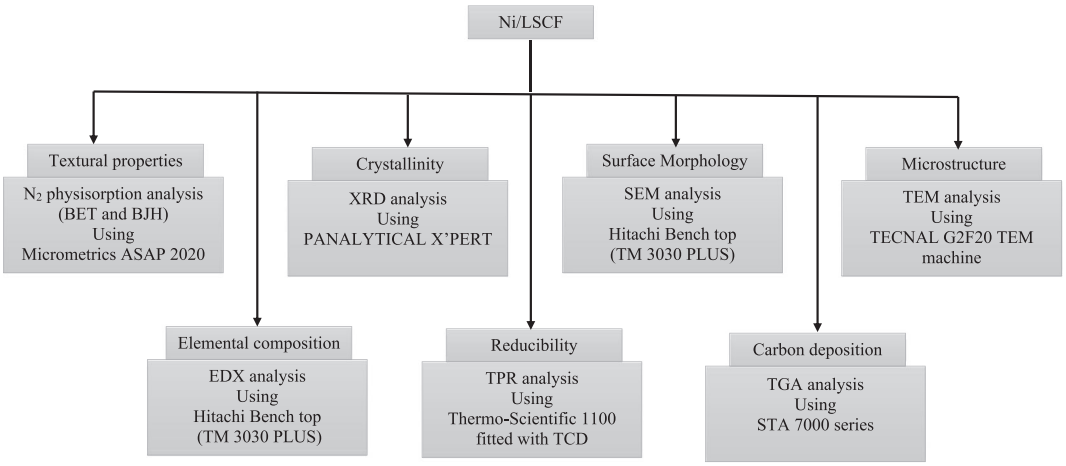

FIGURE 2 Detail methods and instruments used for the determination of the physicochemical properties of the Ni/LSCF catalyst

A five replicate center point (denoted as level 0) was incorporated into the BBD in order to check the experimental variance as well to ensure check of curvature. The data obtained from the BBD were analyzed using Design Expert version 7.2. The parameters and the levels (−1, 0, +1) employed in the design are summarized in Table 1.

The BBD was employed to generate 17 experiments, which are made up of the treatment combinations of the parameters. Each of the treatment conditions was

TABLE 1 Parameters and level investigated using the BBD

Parameters	Unit	Code Symbol	Level and Range		
			−1	0	1
P_{CH_4}	kPa	A	10	20	30
$P_{H_2O(g)}$	kPa	B	10	20	10
T	°C	C	750	800	850

Abbreviation: BBD: Box-Behnken experimental design.

employed to obtain their corresponding responses (CH_4 conversion and the H_2 yield). The schematic representation of the set-up used for obtaining the experimental data for the optimization study is depicted in Figure 3. The feed stream, which was regulated by a mass flow meter (Alicat Scientific Inc, USA), consists of H_2, CH_4, and N_2. The H_2 was employed for the in situ reduction of Ni/LSCF catalyst before initiating the reaction. The CH_4 and steam (obtained from the steam saturator unit) together with the N_2, which serves as the carrier gas, was fed into a tubular reactor made up of stainless steel. The temperature in the reactor was monitored using a K-type thermocouple. The concentration of the gaseous products was measured using gas chromatography with TCD-FID detector (Shimadzu gas chromatography system).

4 | RESULTS AND DISCUSSION

4.1 | Catalyst characterization

The XRD pattern of the Ni/LSCF showing the phase identification is depicted in Figure 4. The diffraction peaks, which can be identified between 24.3° and 78.4°, are corresponds to 110, 131, 119, 025, 122, 113, 213, and 237 plane of hexagonal structure of LSCF perovskite (ICSD: 187793, ICDD: 98-018-7793), which is consistent with previous report on phase identification for LSCF perovskite.[41] It is noteworthy that a small amount of La_2O_3 can be identified from the XRD pattern at 2θ = 74.8° (104). The diffraction peak at 2θ = 43.8° corresponds to 111 plain of NiO (ICSD: 92127, ICDD: 00-044-1159). Interestingly, the formation of orthorhombic phase of $Fe_{0.8}La_1Ni_{0.2}O_3$ in a small amount (ICSD: 158821, ICDD: 98-015-8821) is evidence at 2θ = 67.4° (216).

The morphology of the Ni/LSCF catalyst as captured by the TEM and SEM images and the elemental compositions are represented in Figures 5A to 5C, respectively. The TEM image shows homogeneous spherical Ni nanoparticles intertwined with the LSCF. This implies that the Ni is well dispersed on the on LSCF and there exists a Ni-LSCF interaction between the Ni and the LSCF support, which is consistent with that reported by

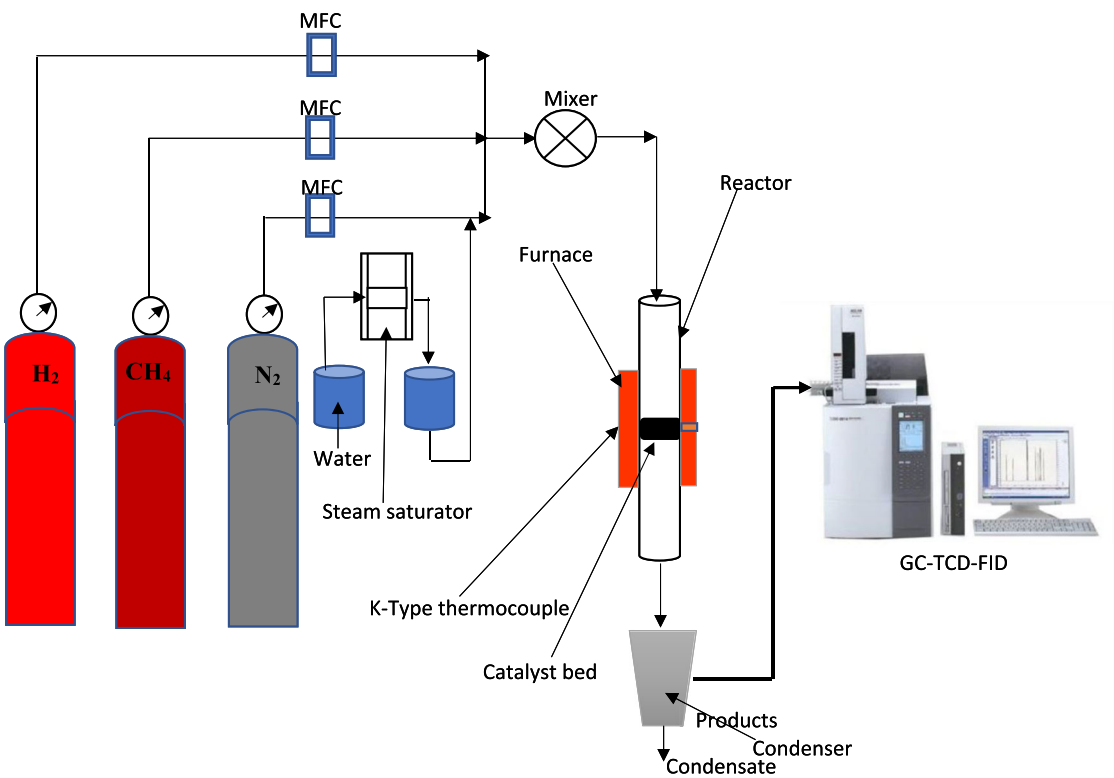

FIGURE 3 Schematic representation of set-up used to obtain experimental data for the optimization study [Colour figure can be viewed at wileyonlinelibrary.com]

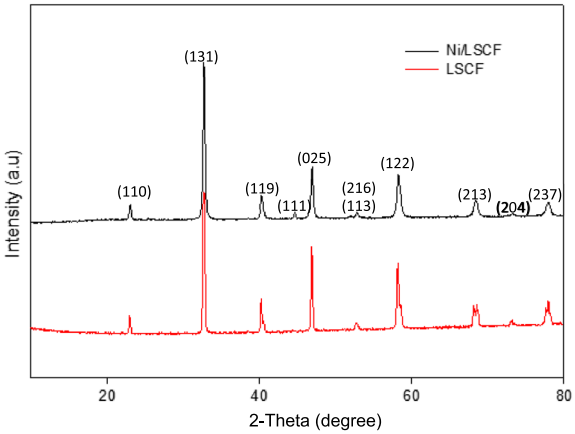

FIGURE 4 X-ray diffraction pattern of the LSCF and Ni/LSCF [Colour figure can be viewed at wileyonlinelibrary.com]

Wolfbeisser et al[42] for Ni/CeO-ZrO_2 catalyst. Furthermore, the dispersion of the Ni on the LSCF is ascertained from the SEM images. The Ni nanoparticles are well dispersed on the LSCF as indicated by the yellow arrows in the SEM image. Although, weak agglomeration of the Ni nanoparticles is evident, which can be attributed to the high calcination temperature.[43] The evidence of the elemental make-up of the Ni/LSCF catalyst is shown in EDX micrograph depicted in Figure 5C. Interestingly, all the elemental components, which include Ni, La, Sr, Co, Fe, and O, are captured by the different peaks in the EDX micrograph. This trend is consistent with the EDX dot mapping depicted in Figure 6 where each of the elements is coded in a unique color to indicate their presence. The atomic percentage of the Ni, La, Sr, Co, Fe, and O were obtained from the EDX as 5.60%, 2.37%, 20.78%, 3.43%, 2.34%, 23.56%, and 44.25%, respectively.

The wide-scan X-ray photoelectron spectroscopy (XPS) spectrum of the Ni/LSCF catalyst is shown in Figure 7. It is notable that all the chemical composition of the Ni/LSCF catalyst is represented in the wide-scan XPS spectrum. The atomic percentage of the observed elements represented as Ni2p3, La3d5, Sr3d5, Co2p, Fe2p3, and O1s at binding energies of 854.70, 836.44, 135.08, 886.40, 710.80, and 529.32 eV were estimated as 5.5%, 24.0%, 4.2%, 4.3%, 10.0%, and 52.0%, respectively. The Ni2p3 can be ascribed to nickel bonded to oxygen in the form of NiO, which is consistent with the XRD analysis. The La3d5, Sr3d4, Co2p, Fe2p3, and O1s could be ascribed to lanthanum, strontium, cobalt, iron, and oxygen bonded in the LSCF perovskite as indicated in the XRD analysis. Moreover, Co2p and Fe2p3 can also be attributed to the cobalt and iron bonded to oxygen resulting in the formation of Co_3O_4 and Fe_2O_3, although not detected from the XRD analysis.

The textural properties of a heterogeneous catalyst in term of the surface area and the porosity play a significant role in the activity of such catalyst. Typically, the absorptivity of a catalyst is a function of the surface area, while the penetration of the analyte molecules (the reactants) into the catalyst pores for inner surface interaction is defined by the pore distributions (pore size and pore volume). Figures 8A and 8B depict the pore distributions of the Ni/LSCF catalyst as a function of the incremental pore volume and the incremental pore area. It is obvious that the pore size is in the range of 2 to 11 nm, which confirms the mesoporous natural of the catalyst.[44] The different peaks observed along the pore widths could be attributed to the particle size distribution of the catalyst.[45] This implies that molecular adsorption varies along the pore width. The BJH adsorption and desorption cumulative pore volumes of the catalyst were estimated 0.0427 and 0.0429 cm^3/g, respectively. While the BJH adsorption and desorption cumulative pore area of the catalyst was estimated as 8.246 and 8.8598 m^2/g, respectively. Interestingly, the Ni/LSCF catalyst can be described as a mesoporous material (since pore diameter > 2 nm) evident from the BJH average pore diameter of 12.08 and 15.17 nm for adsorption and desorption, respectively.[46] The analysis of the adsorption-desorption

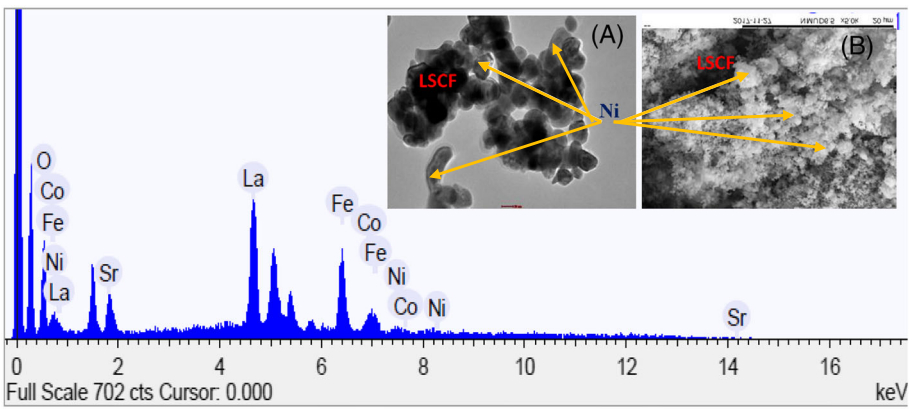

FIGURE 5 Energy-dispersive X-ray spectroscopymicrograph of Ni/LSCF catalyst with inserted (A) transmission electron microscopy images (B) scanning electron microscopy images[36] [Colour figure can be viewed at wileyonlinelibrary.com]

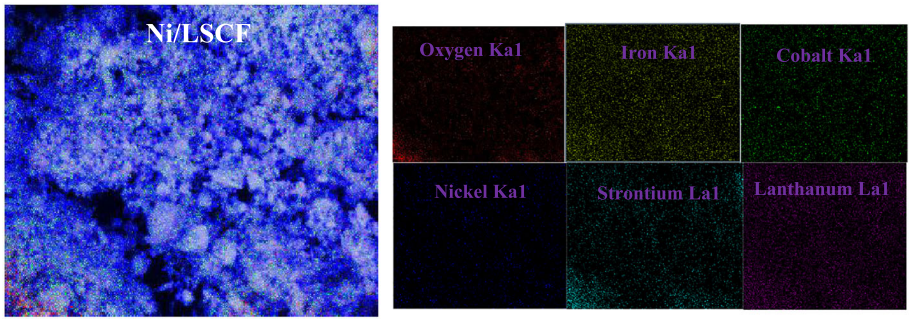

FIGURE 6 Energy-dispersive X-ray spectroscopy dot mapping of the Ni/LSCF catalyst [Colour figure can be viewed at wileyonlinelibrary.com]

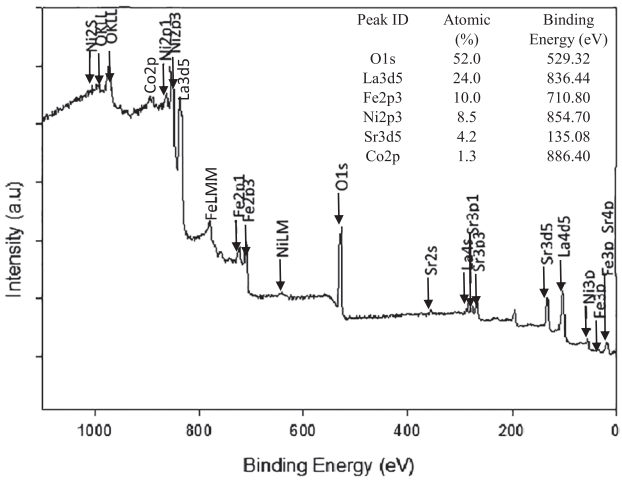

FIGURE 7 Wide-scan X-ray photoelectron spectroscopy spectrum of the Ni/LSCF catalyst. The insert table shows the quantification of all observed elements, atomic percentage, and binding energy

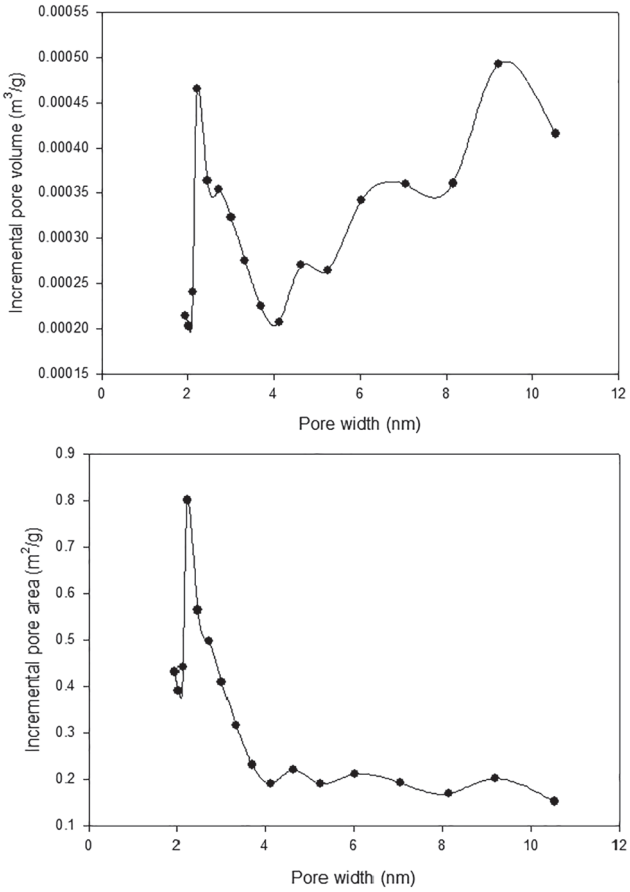

FIGURE 8 The pore distributions of the Ni/LSCF catalyst showing the (A) incremental pore volume and (B) incremental pore area as a function of pore width

isotherms of the Ni/LSCF catalyst resulted in type IV based on the IUPAC classification of adsorption isotherm.[47] The occurrence of type IV adsorption isotherm for the catalyst signifies that the adsorption occurs on mesoporous materials through multilayer adsorption followed by capillary condensation.[48] Moreover, N_2 adsorption-desorption isotherm of the Ni/LSCF catalyst has the attributes of hysteresis loops type H_3, which implies a loose assemblage of plate-like particles with the formation of slit-like pores.[49] The specific surface area of the Ni/LSCF catalyst obtained from the analysis of the adsorption-desorption data using the BET method was estimated as 9.88 m^2/g.

The determination of the extent of reduction of the Ni/LSCF catalyst by H_2-TPR revealed that the NiO oxide formed after the calcination of the catalyst can easily be reduced to Ni° using H_2 probe gas. It is obvious from the XRD analysis that NiO and a small amount of Co_3O_4 were formed. As described in Ayodele et al,[36] the small peak centered at 480°C and the sharp peak centered at 760°C can be attributed to the reduction of NiO and Co_3O_4 species in the catalyst by the H_2 to Co° and Ni. The amount of H_2 utilized for the reduction of the NiO and Co_3O_4 species were estimated as 1.62 and 5.2 mmol/g, respectively. The redox properties exhibited by the Ni/LSCF in this study are consistent with that reported for Cu/LSCF, Ag/LSCF, and Pt/LSCF employed in SOFCs.[50] The authors reported three characteristic peaks at 220, 330, and 830°C signifying the reduction of the Cu, Ag, and Pt oxides, respectively.

TABLE 2 BBD matrix showing the treatment combinations of the parameters and their response

Run No.	A: P_{CH_4}, kPa	B: $P_{H_2O(g)}$, kPa	C: T, ° C	CH_4 Conversion, %	H_2 Yield, %
1	20	20	800	83.52	81.28
2	30	20	750	76.18	75.34
3	10	30	800	82.47	80.72
4	20	20	800	82.52	80.17
5	20	20	800	82.63	80.25
6	30	30	800	84.20	82.52
7	20	30	850	88.87	86.56
8	30	20	850	89.51	86.22
9	10	10	800	81.26	79.65
10	10	20	850	87.08	88.4
11	20	20	800	83.32	81.43
12	10	20	750	75.93	72.94
13	20	10	850	88.87	87.44
14	20	30	750	85.67	73.34
15	30	10	800	82.99	81.56
16	20	10	750	73.44	72.76
17	20	20	800	83.58	81.29

Abbreviation: BBD: Box-Behnken experimental design.

4.2 | The BBD matrix analysis

The different treatment combinations (comprising the three parameters) together with their respective responses obtained from the BBD experimental runs are summarized in Table 2. The different interaction models were investigated by fitting them into the experimental data to generate regression equations that explain the data. Subsequently, the adequacy of the model to represent H_2 production as well as the CH_4 conversion was analyzed using Design-Expert software and summarized in Tables 3 and 4. The analysis of the responses based on the values of coefficient of determination (R^2), adjusted R^2, and the predicted R^2 shows that the quadratic models for the two responses are statistically significant for optimizing H_2 yield and CH_4 conversion. This trend is consistent with previous work where BBD was employed for optimization of CO-rich H_2 production by CH_4 reforming using CO_2 over Co/Sm_2O_3 catalyst.[51] Hence, it can be deduced that an empirical relationship exists between the parameters (P_{CH_4}, $P_{H_2O(g)}$, and T) investigated and the responses (H_2 yield and CH_4 conversion), which are represented by the quadratic equations (5) and (6). Although, the cubic model obtained for the responses has R^2 values higher than that of the quadratic model; however, the predictability responses using the model cannot be ascertained as indicated in Tables 3 and 4. Analysis of variance (ANOVA) and regression analysis were further explored to ensure the reliability of the fitness of the quadratic model as discussed in the subsequent section.

$$H_2 \text{ yield } (\%) = 88.88 + 0.49A + 0.22B + 6.78C - 0.027\,AB - 1.15\,AC - 0.36\,BC + 0.46\,A^2 - 0.24\,B^2 - 0.62\,C^2, \quad (5)$$

$$CH_4 \text{ conversion } (\%) = 83.11 + 0.77\,A + 1.83\,B + 5.39\,C + 0.00035\,AB + 0.55\,AC - 0.3.06BC - 1.21\,A^2 + 0.83\,B^2 + 0.27\,C^2. \quad (6)$$

4.3 | Diagnostic evaluation of the fitted model

The ANOVA results for the quadratic model fittings of the H_2 yield and the CH_4 conversion are summarized in Tables 5 and 6, respectively. It is obvious that the ANOVA results revealed that the quadratic model (Equations 5 and 6) adequately portrays the actual relationship between the input parameters and the responses, which are necessary for an industrial application. Taking into consideration all the process conditions, the RSM model will be suitable for engineers to predict the suitable process parameters required to optimize H_2 production by SMR over the Ni/LSCF catalyst. Statistical parameters such as the *P*-values and the lack of fits were employed as criteria to check the robustness of the quadratic model.

TABLE 3 Model summary statistics for the H_2 yield

Source	Standard Deviation	R^2	Adjusted R^2	Predicted R^2	PRESS	
Linear	2.718409066	0.7946343	0.7472422	0.590677809	191.474	
2FI	2.903647655	0.8197635	0.711621567	0.159456752	393.192	
Quadratic	1.03024581	0.9841169	0.963695818	0.845236787	72.3957	Suggested
Cubic	0.897151046	0.9931175	0.972470008		+	Aliased

Note. + Case(s) with the leverage of 1.0000: prediction error sum of squares (PRESS) statistic not defined.

TABLE 4 Model summary statistics for CH_4 conversion

Source	Standard Deviation	R^2	Adjusted R^2	Predicted R^2	PRESS	
Linear	0.5879	0.7575	0.7016	0.5157	8.9747	
2FI	0.5619	0.8296	0.7274	0.2216	14.4267	
Quadratic	0.5082	0.9625	0.9571	0.8647	25.1070	Suggested
Cubic	0.2571	0.9857	0.9430		+	Aliased

TABLE 5 ANOVA analysis results for the H_2 yield responses fitting to the quadratic model

Response	Source	Sum of Squares	Degree of Freedom	Mean Square	F Value	*P*-value, Prob > *F*	Decision
H_2 yield	Model	16.7254	9.0000	1.8584	7.1963	<.0001	Significant
	A-CH_4 partial pressure	0.5725	1.0000	0.5725	2.2167	.0080	
	B-Steam partial pressure	0.6903	1.0000	0.6903	2.6731	.0046	
	C-Reaction temperature	12.7765	1.0000	12.7765	49.4749	.0002	
	AB	2.1974	1.0000	2.1974	5.6322	.0314	
	AC	1.1881	1.0000	1.1881	4.6007	.0491	
	BC	0.1482	1.0000	0.1482	0.5740	.0334	
	A^2	0.9530	1.0000	0.9530	3.6903	.0962	
	B^2	0.1492	1.0000	0.1492	0.5778	.4720	
	C^2	0.2776	1.0000	0.2776	1.0748	.3343	
	Residual	1.8077	7.0000	0.2582			
	Lack of fit	1.5434	3.0000	0.5145	7.7854	.2381	Nonsignificant
	Pure error	0.2643	4.0000	0.0661			
	Cor total	18.5331	16.0000				

Abbreviation: ANOVA: analysis of variance.

TABLE 6 ANOVA analysis results for the H_2 yield responses fitting to the quadratic model

Response	Source	Sum of Squares	Degree of Freedom	Mean Square	F Value	*P*-value, Prob > F	Decision
CH_4 conversion, %	Model	460.3538	9.0000	51.1504	48.1912	<.0001	Significant
	A-CH_4 partial pressure	3.0381	1.0000	3.0381	2.8623	<.0001	
	B-Steam partial pressure	0.9316	1.0000	0.9316	0.8777	.0038	
	C-Reaction temperature	367.7472	1.0000	367.7472	346.4716	<.0001	
	AB	5.9780	1.0000	5.9780	5.6322	.0494	
	AC	5.2441	1.0000	5.2441	4.9407	.0416	
	BC	0.5329	1.0000	0.5329	0.5021	.0512	
	A^2	5.9550	1.0000	5.9550	5.6105	.0497	
	B^2	1.0079	1.0000	1.0079	0.9495	.0362	
	C^2	72.4546	1.0000	72.4546	68.2629	<.0001	
	Residual	7.4298	7.0000	1.0614			
	Lack of Fit	4.2103	3.0000	1.4034	1.7437	.2961	Not significant
	Pure Error	3.2195	4.0000	0.8049			
	Cor Total	467.7836	16.0000				

Abbreviation: ANOVA: analysis of variance.

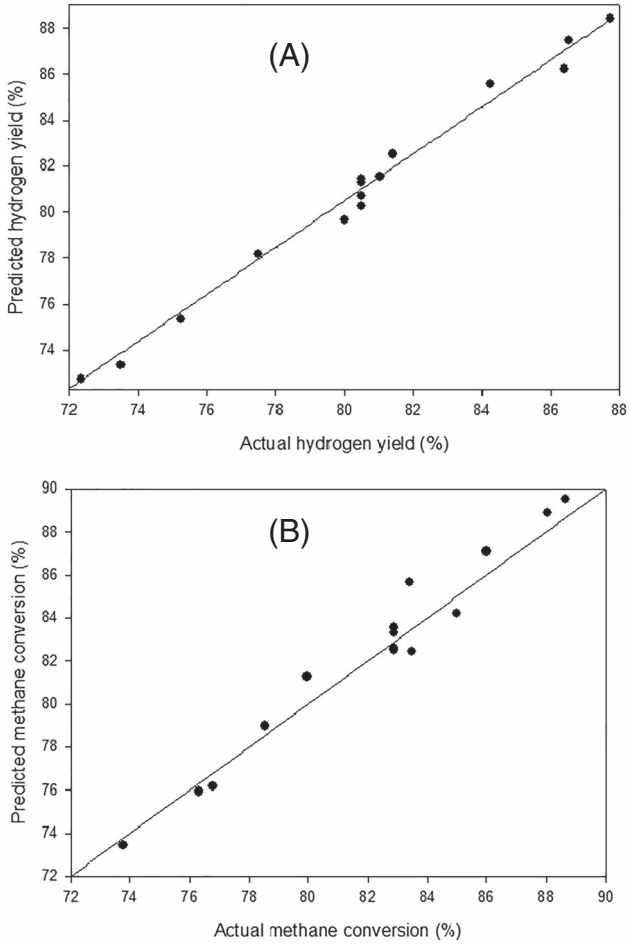

FIGURE 9 Parity plots showing (A) the actual and the predicted H_2 yield (B) actual CH_4 conversion and the predicted CH_4 conversion

Based on the *P*-values <.0001 and.0002 obtained for the H_2 yield and the CH_4 conversions, the two quadratic models can be adjudged to be statistically significant since their respective *P*-values are less than.05 (95% confidence). The *F* tests of values of 7.19 and 48.19 obtained for the H_2 yield and CH_4 conversion implies that the influence of each of the measured factors on the tested quadratic model is within an acceptable limit. A nonsignificant lack of fit with *P*-values of.2381 and.2961 obtained for the H_2 yield and CH_4 conversion, respectively, is an indication that the quadratic model fits well the experimental data.

TABLE 7 Fitting Statistics obtained from the parity plots

Response	Statistical Parameters				
	R	R^2	Adj R^2	Standard Error of Estimate	*P*-value
H_2 yield, %	0.9792	0.9588	0.9561	0.9677	<.0001
CH_4 conversion, %	0.9997	0.9940	0.9926	0.5422	<.0001

A parity (diagnostic) plot was further employed to ascertain the adequacy and suitability of the BBD quadratic model for the optimization of CH_4 conversion and H_2 yield from SMR over Ni-LSCF catalyst. This will enable the evaluation of the correlation between the actual and the BBD predicted values of the responses. Figure 10 depicts the parity plots of the actual values of responses and their respected predicted values from the BBD model. The positioning of the data points close to the straight line are indications of strong correlations between the actual (experimental) data of the responses and the predicted values of the responses obtained from the BBD model. This further strengthens the robustness of the BBD quadratic model to predict treatment combinations for the optimization of the CH_4 conversion and the H_2 yield. The R^2 values of 0.9588 and 0.9940 obtained from the fittings of the data in Figures 9 also confirm that the actual and the predicted values of the responses are

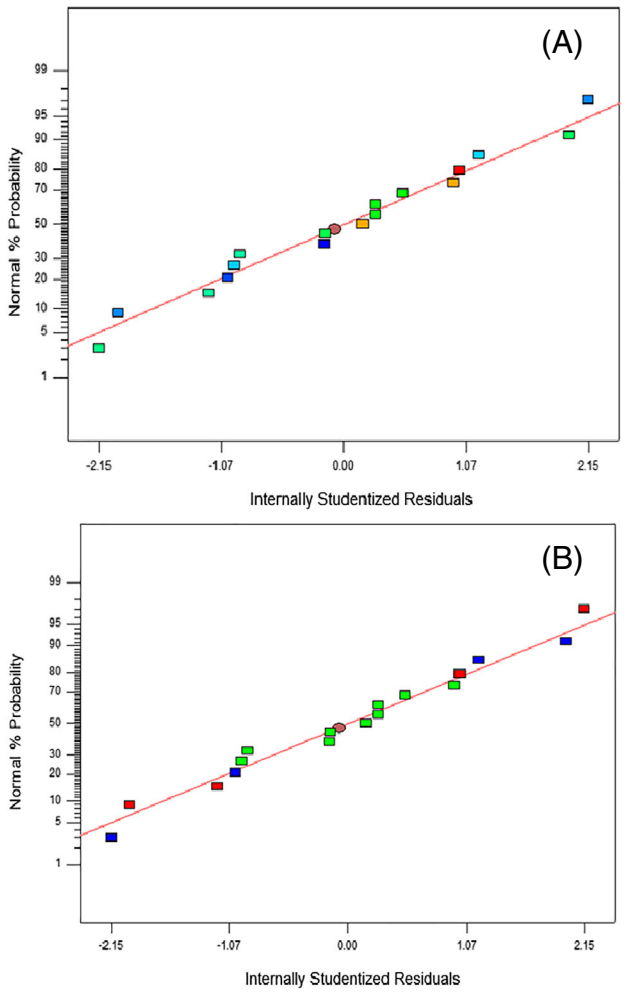

FIGURE 10 Normal probability plots of internally studentized residual for (A) H_2 yield (B) CH_4 conversion [Colour figure can be viewed at wileyonlinelibrary.com]

strongly correlated (Table 7). Besides, *P*-values (<.0001) and the standard error of estimate, which are less than 1 further, confirm the validity of the diagnostic plots.

A further analysis was also performed on the data to examine the normality of the residual. This will enable the assessment of how the data are normally distributed. The normal probability plots, which consist of raw data, residuals derived from model fits, and estimated parameters, were employed to examine the normality of the residual.[52] The use of the internal studentized residuals for the normal probability plots enables the quantification of how large the residuals are in standard deviation units.[52] The normal probability plots obtained for the H_2 yield and CH_4 conversion are presented in Figures 10A and 10B, respectively. Interestingly, the data points are closely aligned to the straight line with minimal scattering signifying that the data are normally distributed.

4.4 | Interaction effects of parameters on H_2 yield

The different treatment combinations of the process parameters obtained from BBD matrix were employed to investigate the optimum process parameters for maximizing H_2 yield. Moreover, the interaction effects of two treatment combinations of the parameters (keeping the third parameter constant) on the responses were studied using a three-dimensional response plot. The response plots of the parameters' interaction effects on SMR on H_2 yield are shown in Figures 11A to 11C. The three process parameters significantly affect the H_2 yield obtained from the SMR (P <.0001). Figure 11A shows that the interaction effects of P_{CH_4} and $P_{H_2O(g)}$ positively influence the H_2 yield in the linear and quadratic terms. This implies that there is a synergistic impact of increasing the P_{CH_4} and $P_{H_2O(g)}$ on the H_2 yield as indicated by the *P*-value of.0394 (P<.05). Moreover, H_2 yield was also significantly affected by the linear interaction between the reaction temperature and P_{CH_4} as shown in Figure 11B. Since the effect of $P_{H_2O(g)}$is constant in this scenario, it can be deduced that CH_4 cracking in primary responsible for the H_2 produced.[53] There is a corresponding increase in H_2 yield as the reaction temperature and P_{CH_4} increases. However, a declined in H_2 yield was observed at 30 kPa and 850°C, which can be attributed to gradual deactivation of the catalyst by carbon deposition.[26] A similar trend was observed for the interaction effect of reaction temperature and $P_{H_2O(g)}$ on H_2 yield shown in Figure 11C. The *P*-value of.0334 (P<.05) from the ANOVA results implies that both reaction temperature and $P_{H_2O(g)}$significantly affected H_2 yield. However, it can be inferred that the H_2 production from the

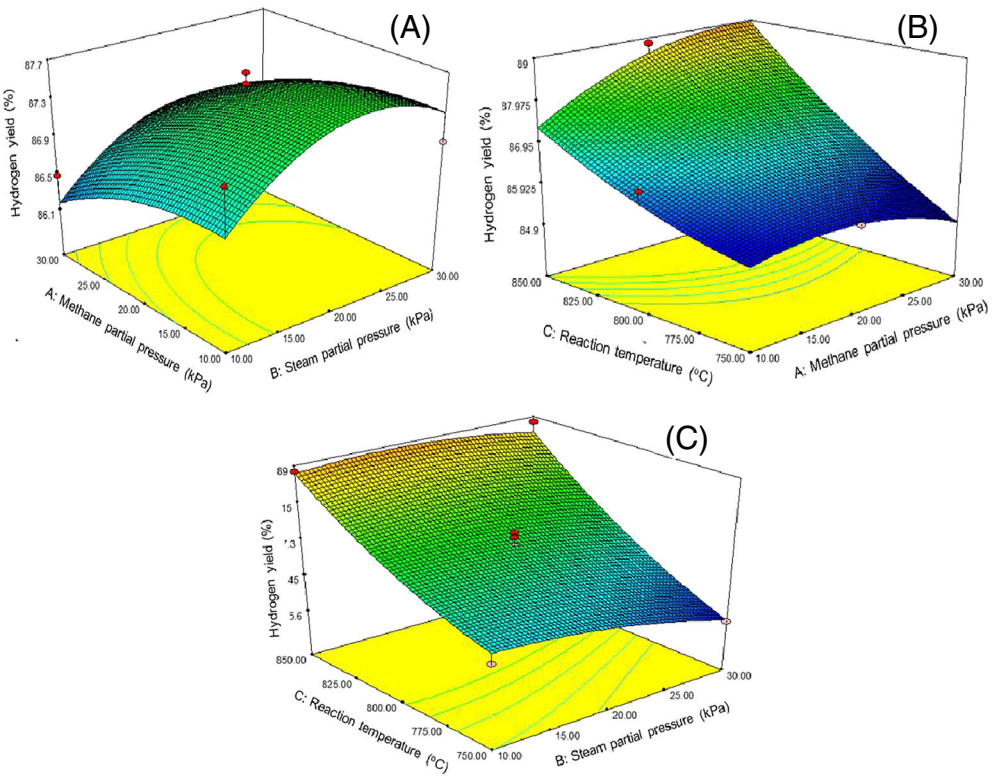

FIGURE 11 Response plots showing the interaction effect of (A) P_{CH_4} and $P_{H_2O(g)}$, (B) reaction temperature and P_{CH_4}, and (C) of reaction temperature and $P_{H_2O(g)}$ on H_2 yield [Colour figure can be viewed at wileyonlinelibrary.com]

interaction of reaction temperature and $P_{H_2O(g)}$ is mainly by water splitting as reported by Sheu et al.[54]

4.5 | Interaction effect of the parameters on CH_4 conversion

The interaction effects of P_{CH_4}, $P_{H_2O(g)}$, and reaction temperature on CH_4 conversion are depicted in Figures 12A to 12C. The three parameters have significant effects on the CH_4 conversion as indicated by the P-value (<.0001). Besides, the individual effect of each of the parameters is positive and significant as indicated by the P-values, which are less than.05. Figure 12A shows that P_{CH_4} and $P_{H_2O(g)}$ have a synergistic and significant effect on the CH_4 conversion (P<.0001). The CH_4 conversion increases with an increase in both P_{CH_4} and $P_{H_2O(g)}$ until it attains the maximum values. However, since the P-value of P_{CH_4} (P<.0001) is less than that of $P_{H_2O(g)}$ (P =.0038), it implies that the P_{CH_4} has a greater influence on the CH_4 conversion. Similarly, there is a significant effect of the interaction between the reaction temperature and P_{CH_4} on the CH_4 conversion as indicated in Figure 12B. The increase in reaction temperature and P_{CH_4} leads to a corresponding increase in the CH_4 conversion. Interestingly, the same P-values (<.0001) were obtained from the ANOVA results for the reaction temperature and the P_{CH_4} an indication that both parameters have an equal impact on the CH_4 conversion. The response plot is shown in Figure 12C revealed that both reaction temperature and $P_{H_2O(g)}$ have a significant effect on the CH_4 conversion. However, the P-value of.051 obtained for the interaction of both parameters (reaction temperature and $P_{H_2O(g)}$) is marginally significant (since P is approximately equal to.05).

4.6 | Determination of optimum conditions using desirability function

One of the major challenges in industrial processes is that product performance is often characterized by more than one response, which usually leads to the constraint of simultaneous optimization. For effective quality control and process improvement, it is expedient to optimize the process parameters being used for industrial operations of SMR to H_2. The desirability approach was applied to determine the optimum parameters that can maximize

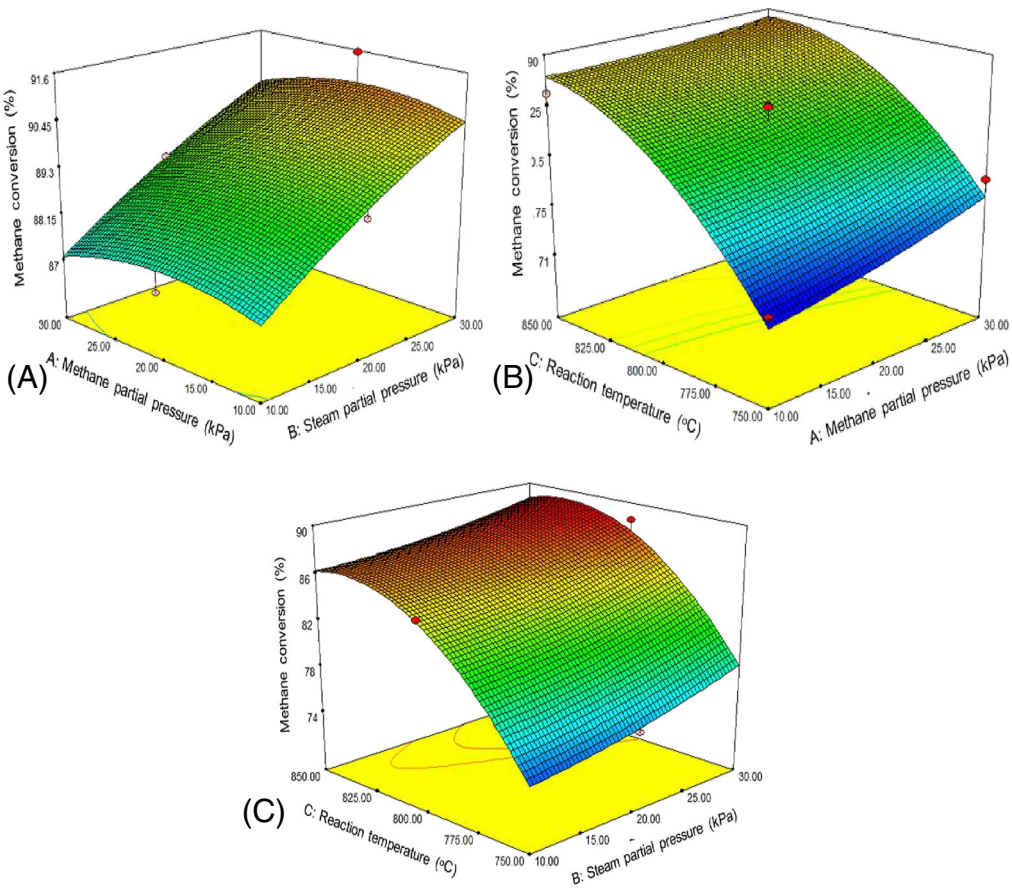

FIGURE 12 Response plots showing the effects (A) P_{CH_4} and $P_{H_2O(g)}$, (B) reaction temperature and P_{CH_4}, and (C) of reaction temperature and $P_{H_2O(g)}$ on CH_4 conversion [Colour figure can be viewed at wileyonlinelibrary.com]

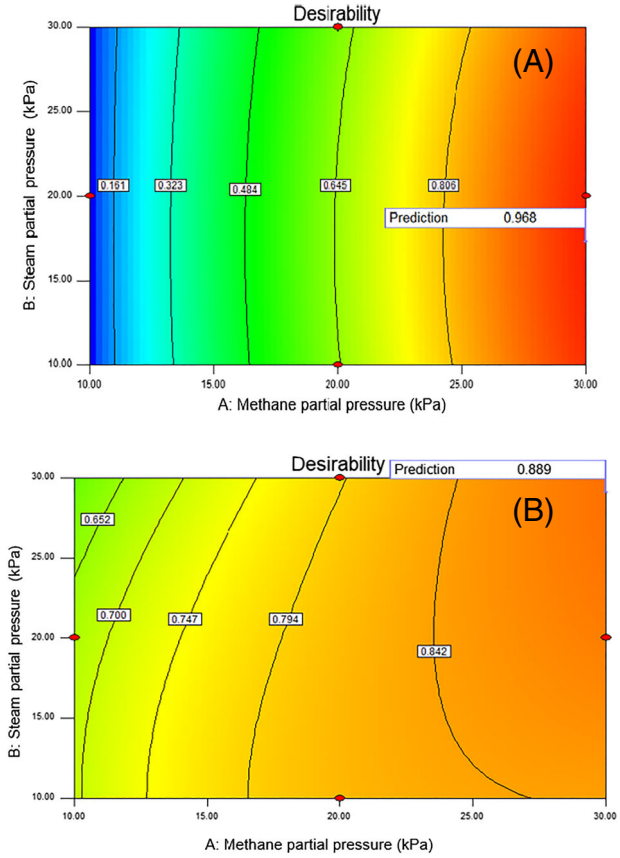

FIGURE 13 Desirability function contour plots for the selection of optimum process conditions for (A) H_2 yield and (B) CH_4 conversion [Colour figure can be viewed at wileyonlinelibrary.com]

H_2 yield and CH_4 conversion.[55] The use of the desirability approach in hinged on its popularity in the industries for the optimization of multiple response processes.[56] The desirability function is based on the principle that for any of the responses of an industrial process or product to be in the desired limit, the overall desirability function must be desirable. The use of the desirability approach entails the search for a set of process conditions that offer the most desirable responses. The desirability function contour plots of the H_2 yield and the CH_4 conversion showing different optimum predictions are depicted in Figures 13A and 13B, respectively. The near-optimum region for the H_2 yield was located at the center of the 30-kPa grid line having maximum H_2 yield desirability of 0.968. Similarly, the near-optimum region for the CH_4 conversion was also located at the center of the 30-kPa grip line having maximum CH_4 conversion desirability of 0.889. The optimum parameters for the two responses (the H_2 yield and CH_4 conversion) were performed by setting the criteria in Table 8 for obtaining the optimum desirability value. The optimization of the responses using the set criteria resulted in 36 sets of solutions ranked according to their respective desirability as summarized in Table 9. Six sets of solutions (Number 1-6) have the highest values of the response desirability of 0.8894. However, the maximum values of 89.77% and 89.01% were obtained for H_2 yield and CH_4 conversion, respectively, at the optimum values of 30.00 kPa, 28.86 kPa, and 850°C for P_{CH_4}, $P_{H_2O(g)}$, and reaction temperature, respectively.

4.7 | Validation of optimum process parameters

The parameters obtained from the six sets of solutions with the highest desirability in Table 9 were subsequently used to validate the robustness of the BBD model. Experimental runs were made using the values of the parameters combinations in order to obtain a new set of responses (H_2 yield and CH_4 conversion). Moreover, each of the experimental runs was repeated three times to ensure reliability and accuracy. Statistical parameters such as mean absolute percent error (MAPE) represented in the equation below was employed to examine the accuracy of the BBD predictive model.

$$\mathrm{MAPE} = \frac{1}{n}\sum\frac{|\text{Actual values} - \text{Predicted values}|}{|\text{Actual values}|} \times 100, \tag{7}$$

where n is the total number of data.

The values of the responses obtained from the validation experimental runs in comparison with the BBD

TABLE 8 Criteria employed for the optimum desirability function

Parameter	Goal	Lower Limit	Upper Limit	Lower Weight	Upper Weight	Importance
P_{CH_4}, kPa	is in range	10	30	1	1	3
$P_{H_2O(g)}$, kPa	is in range	10	30	1	1	3
T, °C	is in range	750	850	1	1	3
CH_4 conversion, %	maximize	72.76	90.00	1	1	5
H_2 yield, %	maximize	85.67	89.51	1	1	5

TABLE 9 Combinations of optimum process parameters based on desirability values

Input Process Parameters				Predicted Response			
Number	**P_{CH_4}, kPa**	**$P_{H_2O(g)}$, kPa**	**T, °C**	**CH_4 Conversion, %**	**H_2 Yield, %**	**Desirability**	**Decision**
1	30.00	29.10	850.00	89.77	89.00	0.8894	
2	**30.00**	**28.86**	**850.00**	**89.77**	**89.01**	**0.8894**	**Selected**
3	30.00	29.00	850.00	88.45	89.01	0.8894	
4	30.00	29.51	850.00	88.56	88.98	0.8894	
5	30.00	29.65	850.00	88.59	88.98	0.8894	
6	30.00	28.40	850.00	88.33	89.03	0.8894	
7	30.00	28.13	850.00	88.27	89.04	0.8893	
8	30.00	27.18	850.00	88.09	89.08	0.8888	
9	30.00	26.81	850.00	88.02	89.10	0.8885	
10	30.00	26.47	850.00	87.96	89.11	0.8882	
11	29.78	29.11	850.00	88.41	89.01	0.8880	
12	30.00	25.71	850.00	87.82	89.13	0.8875	
13	29.73	27.84	850.00	88.14	89.06	0.8874	
14	30.00	28.59	849.54	88.39	89.00	0.8871	
15	30.00	25.36	850.00	87.76	89.14	0.8870	
16	30.00	24.88	849.99	87.68	89.16	0.8864	
17	30.00	30.00	849.38	88.70	88.93	0.8861	
18	29.16	28.94	850.00	88.20	89.02	0.8838	
19	30.00	24.10	849.22	87.59	89.14	0.8818	
20	29.34	20.85	850.00	86.96	89.25	0.8760	
21	30.00	19.18	850.00	86.88	89.26	0.8749	
22	30.00	30.00	846.97	88.83	88.81	0.8732	
23	30.00	18.40	850.00	86.80	89.26	0.8728	
24	30.00	18.18	849.95	86.78	89.26	0.8720	
25	30.00	17.21	850.00	86.68	89.26	0.8694	
26	29.09	26.81	847.11	87.93	88.97	0.8691	
27	30.00	22.21	846.67	87.43	89.06	0.8671	
28	26.49	19.11	850.00	86.41	89.25	0.8590	
29	25.77	19.97	850.00	86.40	89.23	0.8560	
30	30.00	13.00	850.00	86.38	89.23	0.8557	
31	29.96	12.91	850.00	86.37	89.23	0.8553	
32	30.00	12.59	850.00	86.36	89.22	0.8542	
33	24.74	22.68	850.00	86.52	89.15	0.8506	
34	30.00	11.28	850.00	86.30	89.20	0.8494	
35	24.92	10.04	850.00	86.25	89.11	0.8377	
36	17.93	10.00	847.51	87.28	88.57	0.7969	

The boldface is the optimum conditions that resulted in the maximum values of H_2 yield and CH_4 conversion.

predicted values are summarized in Table 10. It can be seen that there is a close agreement between the actual values of the responses and the BBD predicted values of the responses. The MAPE was found to lie between 0.0562% and 0.7076%, which is relatively small. Hence, it can be inferred that the BBD model is robust for excellent prediction of H_2 yield and CH_4 conversion from SMR over Ni/LSCF catalyst.

TABLE 10 BBD model validation using the combinations of the optimum parameters

Responses	BBD Predictive Values	Actual Values From the Experimental Runs	Desirability	Prediction Error (MAPE, %)
H_2 yield, %	89.00	89.15 ± 0.10	0.8894	0.1685
	89.01	89.25 ± 0.14	0.8894	0.2696
	89.01	88.85 ± 0.12	0.8894	0.1798
	88.98	88.65 ± 0.13	0.8894	0.3709
	88.98	89.03 ± 0.14	0.8894	0.0562
	89.03	88.45 ± 0.12	0.8894	0.7076
CH_4 conversion, %	89.77	88.45 ± 0.12	0.8894	1.4704
	89.77	89.32 ± 0.14	0.8894	0.5013
	88.45	89.05 ± 0.13	0.8894	0.6783
	88.56	88.25 ± 0.11	0.8894	0.3500
	88.59	88.45 ± 0.16	0.8894	0.1580
	88.33	89.05 ± 0.11	0.8894	0.8151

Abbreviations: BBD: Box-Behnken experimental design; MAPE: mean absolute percent error.

4.8 | Stability test of the Ni-LSCF catalyst at the optimum parameters

One of the main challenges in steam reforming is catalyst deactivation. In order to examine the potency of the Ni-LSCF catalyst to deactivation, the optimum values of the process parameters (30.00 kPa, 28.86 kPa, and 850°C) were further employed to perform a stability test. Using the set parameters, the experimental runs for the stability test were performed for 480-minute time-on-stream. The catalyst stability was measured based on the percentage deactivation as well as the values of H_2 yield and CH_4 conversion obtain with time-on-stream. The activity and the deactivation of the Ni-LSCF catalyst with TOS are represented in Figure 14. It is noteworthy that the catalyst was relatively stable between 120 and 360 min. However, a sharp decline in the values of the H_2 yield and CH_4 conversion can be observed from 390 minutes, which is attributed to deactivation of the catalyst site by carbon deposition. Interestingly, the percentage deactivation increases with TOS with the highest values of 8.22% obtained at 480 min which further substantiate the catalyst deactivation.

4.9 | Characterization of the used Ni/LSCF catalyst at the optimum process parameters

The used NI/LSCF catalysts at the optimum parameters were characterized to determine the degree of the catalyst deactivation using TGA, TEM, SEM, and EDX. The TGA profile showing the TG and the DTG curves obtained from the analysis of used Ni-LSCF catalyst is shown in Figure 15. The weight loss denoted by peaks I and II at 110 and 170°C, respectively, can be attributed to carbon formation on the surface of the used catalyst. The TGA analysis shows that 0.53 mg of carbon were deposited per 5.5 mg of used

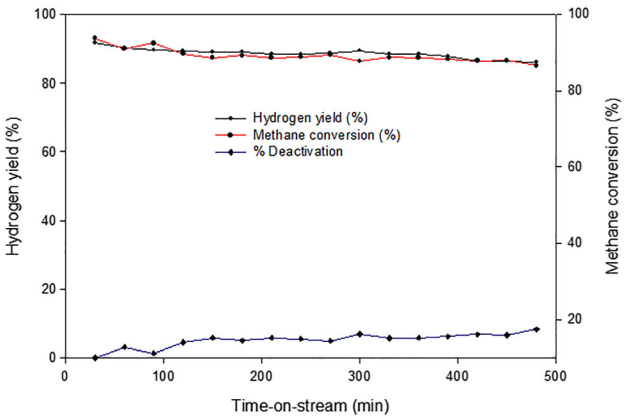

FIGURE 14 Stability test of the Ni/LSCF catalyst at optimum conduction [Colour figure can be viewed at wileyonlinelibrary.com]

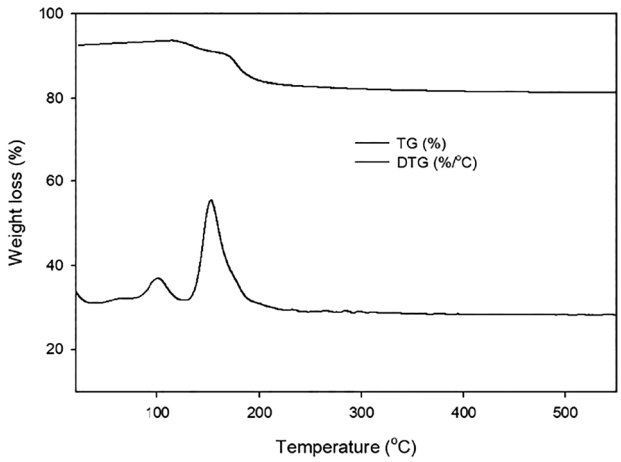

FIGURE 15 Results of thermogravimetric analysis analysis of the used Ni/LSCF catalyst

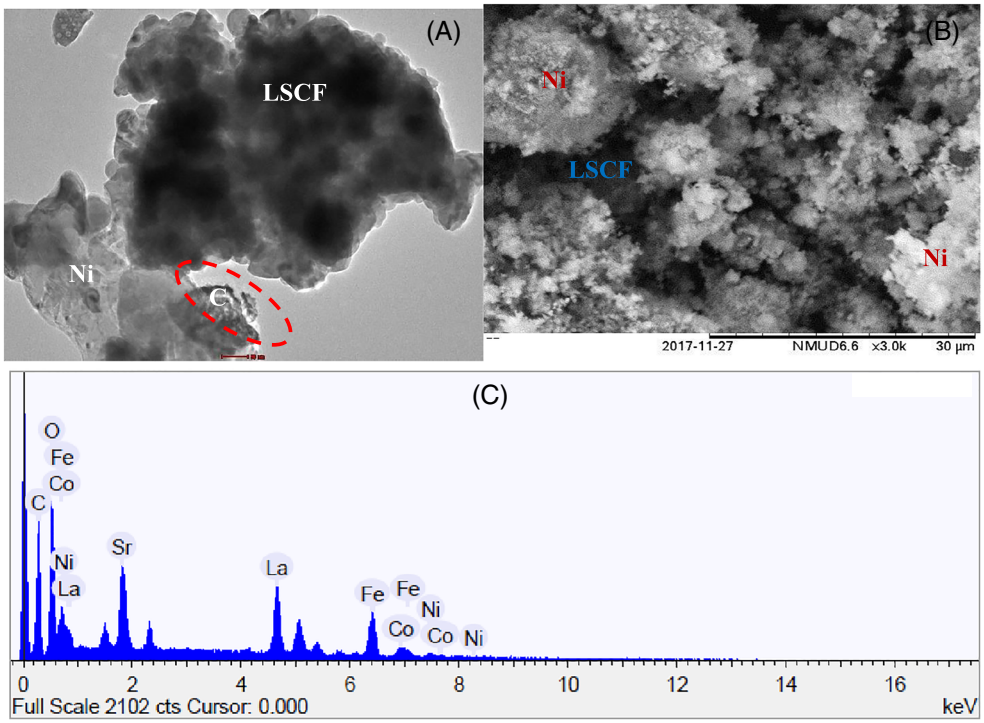

FIGURE 16 (A) Transmission electron microscopy image, (B) scanning electron microscopyimage, and (C) energy-dispersive X-ray spectroscopy micrograph of the used Ni/LSCF catalyst [Colour figure can be viewed at wileyonlinelibrary.com]

catalyst. Further analysis to ascertain the extent of deposition of carbon on the surface of the used catalyst was performed using TEM, SEM, and EDX (Figures 16A-16C). Based on the TEM image, it is obvious that the Ni/LSCF still retains its elemental composition. The Ni nanoparticles were not affected by the little amount of carbon deposited. Since LSCF is a form of O_2 carrier, the release of surface O_2 facilitates the gasification of the deposited carbon. However, if the rate of gasification of the carbon is not balanced with the rate at which the O_2 is released, this might leads to net carbon deposition. This could explain why a small amount of whiskey-type of carbon is seen from the TEM image (Figure 16A). The SEM image of the used Ni/LSCF shown in Figure 16B at the optimum conditions further established the stability of the catalyst based on the presence of the Ni and LSCF. The carbon deposited and the complete elemental composition of the used Ni/LSCF catalyst at the optimum conditions was adequately captured by the EDX micrograph represented in Figure 16C. Besides the presence of elemental carbon, all the elemental make-up of the Ni/LSCF was intact, evidence that the catalyst structure was not affected.

5 | CONCLUSIONS

SMR is a well-matured technological route for H_2 production over Ni-supported catalysts. However, there is a quest for continuous improvement on the process performance in order to enhance process efficiency without increasing cost and time. In order to obtain suitable process conditions to optimize H_2 production, RSM and BBD have been employed to investigate the individual and interaction effects of three parameters, namely, CH_4 partial pressure, steam partial pressure, and reaction temperature on H_2 yield and CH_4 conversion in SMR over Ni/LSCF catalyst. The experimental data obtained from the BBD matrix fitted well into the second-order quadratic model. Statistical parameters such as normality of residuals, ANOVA, and lack of fit were employed to test the adequacy of the model. The normality test revealed that the data used to develop the model were normally distributed, while the response surface models obtained for the H_2 yield and the CH_4 conversion were statistically significant (P <.0001) with the three parameters having significant effects on the responses. A nonsignificant lack of fit was obtained for the response surface model, an indication that the data appropriately fit the model. At optimum conditions (CH_4 partial pressure of 30 kPa, steam partial pressure of 28.91 kPa, and reaction temperature of 850°C), maximum H_2 yield and CH_4 conversion of 89.77% and 89.01% were obtained respectively. The obtained optimum conditions in this study could serve as a guide for setting appropriate parameters for effective H_2 production by SMR over Ni/LSCF catalyst in industrial applications. In addition, the stability of the Ni/LSCF catalysts displayed at the optimum conditions with evidence of little amount of carbon deposition will be suitable for continuous H_2 production

and minimize the cost associated with changing catalytic system. Ascertaining the reusability of the Ni/LSCF catalyst at the optimum conditions could serve as a basis for further investigation on the development of Ni-based catalysts for SMR to H_2.

ACKNOWLEDGEMENTS

This work is supported by Universiti Malaysia Pahang internal grant (vot. RDU150397).

ORCID

Bamidele Victor Ayodele https://orcid.org/0000-0002-7200-3126

REFERENCES

1. Dincer I, Acar C. Review and evaluation of hydrogen production methods for better sustainability. *Int J Hydrogen Energy*. 2015; 40(34):11094-11111.
2. Ahmed A, Al-Amin AQ, Ambrose AF, et al. Hydrogen fuel and transport system: a sustainable and environmental future. *Int J Hydrogen Energy*. 2016;41(3):1369-1380.
3. Staffel I, Scamman D, Abad AV, et al. The role of hydrogen and fuel cells in the global energy system. *Energ Environ Sci*. 2019; 12(2):463-491.
4. Dutta S. A review on production, storage of hydrogen and its utilization as an energy resource. *J Ind Eng Chem*. 2014;20(4): 1148-1156.
5. Baroutaji A, Wilberforce T, Ramadan M, Olabi AG. Comprehensive investigation on hydrogen and fuel cell technology in the aviation and aerospace sectors. *Renew Sustain Energy Rev*. 2019;106:31-40.
6. Dodds PE, Staffell I, Hawkes AD, et al. Hydrogen and fuel cell technologies for heating: A review. *Int J Hydrogen Energy*. 2015;40(5):2065-2083.
7. Verhelst S. Recent progress in the use of hydrogen as a fuel for internal combustion engines. *Int J Hydrogen Energy*. 2014;39(2): 1071-1085.
8. Shahhosseini HR, Iranshahi D, Saeidi S, Pourazadi E, Klemeš JJ. Multi-objective optimisation of steam methane reforming considering stoichiometric ratio indicator for methanol production. *J Clean Prod*. 2018;180:655-665.
9. Esteves NB, Sigal A, Leiva EPM, Rodríguez CR, Cavalcante FSA, De Lima LC. Wind and solar hydrogen for the potential production of ammonia in the state of Ceará - Brazil. *Int J Hydrogen Energy*. 2015;40(32):9917-9923.
10. Chapman A, Itaoka K, Hirose K, et al. A review of four case studies assessing the potential for hydrogen penetration of the future energy system. *Int J Hydrogen Energy*. 2019;44(13):6371-6382.
11. Al-Zareer M, Dincer I, Rosen MA. Analysis and assessment of a hydrogen production plant consisting of coal gasification, thermochemical water decomposition and hydrogen compression systems. *Energ Conver Manage*. 2018;157:600-618.
12. Sengodan S, Lan R, Humphreys J, et al. Advances in reforming and partial oxidation of hydrocarbons for hydrogen production and fuel cell applications. *Renew Sustain Energy Rev*. 2018;82: 761-780.
13. Goto Y, Hisatomi T, Wang Q, et al. A particulate photocatalyst water-splitting panel for large-scale solar hydrogen generation. *Joule*. 2018;2(3):509-520.
14. Hsu SH, Miao J, Zhang L, et al. An Earth-abundant catalyst-based seawater photoelectrolysis system with 17.9% solar-to-hydrogen efficiency. *Adv Mater*. 2018;30:1-8.
15. Jin F, Sun H, Wu C, et al. Effect of calcium addition on Mg-AlOx supported Ni catalysts for hydrogen production from pyrolysis-gasification of biomass. *Catal Today*. 2018;309:2-10.
16. Parthasarathy P, Narayanan KS. Hydrogen production from steam gasification of biomass: Influence of process parameters on hydrogen yield – A review. *Renew Energy*. 2014;66:570-579.
17. Roh H-S, Koo KY, Jung UH, Yoon WL. Hydrogen production from natural gas steam reforming over Ni catalysts supported on metal substrates. *Curr Appl Phys*. 2010;10(2):S37-S39.
18. Alam S, Kumar JP, Rani KY, Sumana C. Self-sustained process scheme for high purity hydrogen production using sorption enhanced steam methane reforming coupled with chemical looping combustion. *J Clean Prod*. 2017;162:687-701.
19. Chen CC, Tseng HH, Lin YL, Chen WH. Hydrogen production and carbon dioxide enrichment from ethanol steam reforming followed by water gas shift reaction. *J Clean Prod*. 2017;162: 1430-1441.
20. Abdullah B, Abd Ghani NA, Vo DVN. Recent advances in dry reforming of methane over Ni-based catalysts. *J Clean Prod*. 2017;162:170-185.
21. Palma V, Ricca A, Meloni E, Martino M, Miccio M, Ciambelli P. Experimental and numerical investigations on structured catalysts for methane steam reforming intensification. *J Clean Prod*. 2016;111:217-230.
22. Iulianelli A, Liguori S, Wilcox J, Basile A. Advances on methane steam reforming to produce hydrogen through membrane reactors technology: A review. *Catal Rev - Sci Eng*. 2016;58(1):1-35.
23. Nieva MA, Villaverde MM, Monzón A, Garetto TF, Marchi AJ. Steam-methane reforming at low temperature on nickel-based catalysts. *Chem Eng J*. 2014;235:158-166.
24. Qi Y, Cheng Z, Zhou Z. Steam reforming of methane over Ni catalysts prepared from hydrotalcite-type precursors: catalytic activity and reaction kinetics. *Chin J Chem Eng*. 2015;23(1):76-85.
25. Jones G, Jakobsen JG, Shim SS, et al. First principles calculations and experimental insight into methane steam reforming over transition metal catalysts. *J Catal*. 2008;259(1):147-160.
26. Sehested J. Four challenges for nickel steam-reforming catalysts. *Catal Today*. 2006;111(1-2):103-110.
27. Wang K, Dou B, Jiang B, et al. Effect of support on hydrogen production from chemical looping steam reforming of ethanol over Ni-based oxygen carriers. *Int J Hydrogen Energy*. 2016;1-14.
28. Maluf SS, Assaf EM. Ni catalysts with Mo promoter for methane steam reforming. *Fuel*. 2009;88(9):1547-1553.
29. Rajesh JK, Gupta SK, Rangaiah GP, Ray AK. Multiobjective optimization of steam reformer performance using genetic algorithm. *Ind Eng Chem Res*. 2000;39(3):706-717.

30. Lian J, Fang X, Liu W, et al. Ni Supported on LaFeO3 Perovskites for methane steam reforming: on the promotional effects of plasma treatment in H2--Ar atmosphere. *Top Catal*. 2017; 60(12-14):831-842.

31. Yang Q, Liu G, Liu Y. Perovskite-type oxides as the catalyst precursors for preparing supported metallic nanocatalysts: a review. *Ind Eng Chem Res*. 2018;57:17.

32. Raheem A, Ji G, Memon A, et al. Catalytic gasification of algal biomass for hydrogen-rich gas production: parametric optimization via central composite design. *Energ Conver Manage*. 2018; 158:235-245.

33. Patcharavorachot Y, Chatrattanawet N, Arpornwichanop A, Assabumrungrat S. Optimization of hydrogen production from three reforming approaches of glycerol via using supercritical water with in situ CO 2 separation. *Int J Hydrogen Energy*. 2019;44(4):2128-2140.

34. Azizzadeh Fard A, Arvaneh R, Alavi SM, Bazyari A, Valaei A Propane steam reforming over promoted Ni–Ce/MgAl2O4 catalysts: effects of Ce promoter on the catalyst performance using developed CCD model. *Int J Hydrogen Energy*. Epub ahead of print 2019. DOI: https://doi.org/10.1016/j.ijhydene.2019.06.100, 44, 39, 21607, 21622.

35. Ayodele BV, Abdullah S. An overview of response surface methodology approach to optimization of hydrogen and syngas production by catalytic reforming of greenhouse gases (CH4 and CO2). In: *Statistical Approaches With Emphasis on Design of Experiments Applied to Chemical Processes*:65-78.

36. Ayodele BV, Yassin MY, Naim R, Abdullah S. Hydrogen production by thermo-catalytic conversion of methane over lanthanum strontium cobalt ferrite (LSCF) and αAl2O3 supported Ni catalysts. *J Energy Inst*. 2019;92(4):892-903.

37. Jiang SP. A review of wet impregnation—An alternative method for the fabrication of high performance and nano-structured electrodes of solid oxide fuel cells. *Mater Sci Eng A*. 2006; 418(1-2):199-210.

38. Ayodele B V., Cheng CK. Modelling and optimization of syngas production from methane dry reforming over ceria-supported cobalt catalyst using artificial neural networks and Box–Behnken design. *J Ind Eng Chem*. Epub ahead of print September 2015. DOI: https://doi.org/10.1016/j.jiec.2015.08.021, 32, 246, 258.

39. Meryemoğlu B, Hasanoğlu A, Kaya B, et al. Hydrogen production from aqueous-phase reforming of sorghum biomass: an application of the response surface methodology. *Renew Energy*. 2014;62:535-541.

40. Zolgharnein J, Shahmoradi A, Ghasemi JB. Comparative study of Box-Behnken, central composite, and Doehlert matrix for multivariate optimization of Pb (II) adsorption onto Robinia tree leaves. *J Chemometr*. 2013;27(1-2):12-20.

41. Fan B, Yan J, Yan X. The ionic conductivity, thermal expansion behavior, and chemical compatibility of La0.54Sr0.44Co0.2Fe0.8O3-δ as SOFC cathode material. *Solid State Sci*. 2011;13(10): 1835-1839.

42. Wolfbeisser A, Sophiphun O, Bernardi J, Wittayakun J, Föttinger K, Rupprechter G. Methane dry reforming over ceria-zirconia supported Ni catalysts. *Catal Today*. 2016;277:234-245.

43. Serrano-Lotina A, Daza L. Influence of the operating parameters over dry reforming of methane to syngas. *Int J Hydrogen Energy*. 2014;39(8):4089-4094.

44. Gupta VK, Gupta B, Rastogi A, Agarwal S, Nayak A. A comparative investigation on adsorption performances of mesoporous activated carbon prepared from waste rubber tire and activated carbon for a hazardous azo dye—Acid Blue 113. *J Hazard Mater*. 2011;186(1):891-901.

45. Jabłoński M. Influence of particle size distribution on thermokinetics of ilmenite with sulphuric acid reaction. *J Therm Anal Calorim*. 2009;96(3):971-977.

46. Branton PJ, Hall PG, Sing KSW. Physisorption of nitrogen and oxygen by MCM-41, a model mesoporous adsorbent. *J Chem Soc Chem Commun*. 1993;(16):1257-1258.

47. Connelly NG, Damhus T, Hartshorn RM, Hutton AT. Nomenclature of inorganic chemistry IUPAC recommendations. *R Soc Chem*. 2005;27:(6)25-26.

48. Kim JM, Stucky GD. Synthesis of highly ordered mesoporous silica materials using sodium silicate and amphiphilic block copolymers. *Chem Commun*. 2000;(13):1159-1160.

49. Sing KSW, Williams RT. Physisorption hysteresis loops and the characterization of nanoporous materials. *Adsorpt Sci Technol*. 2004;22(10):773-782.

50. Huang TJ, Shen XD, Chou CL. Characterization of Cu, Ag and Pt added La0.6Sr0.4Co0.2Fe0.8O3-δ and gadolinia-doped ceria as solid oxide fuel cell electrodes by temperature-programmed techniques. *J Power Sources*. 2009;187(2):348-355.

51. Ayodele B V., Khan MR, Nooruddin SS, et al. Modelling and optimization of syngas production by methane dry reforming over samarium oxide supported cobalt catalyst: response surface methodology and artificial neural networks approach. *Clean Technol Environ Policy*. Epub ahead of print 2016. DOI: https://doi.org/10.1007/s10098-016-1318-5, 19:(4) 1181-1193.

52. Jarque CM, Bera AK. A test for normality of observations and regression residuals. *Int Stat Rev/Rev Int Stat*. 1987;55(2):163-172.

53. Abánades A, Rubbia C, Salmieri D. Thermal cracking of methane into Hydrogen for a CO2-free utilization of natural gas. *Int J Hydrogen Energy*. 2013;38(20):8491-8496.

54. Sheu EJ, Mokheimer EMA, Ghoniem AF. A review of solar methane reforming systems. *Int J Hydrogen Energy*. 2015; 40(38):12929-12955.

55. Wang J, Wan W. Application of desirability function based on neural network for optimizing biohydrogen production process. *Int J Hydrogen Energy*. 2009;34(3):1253-1259.

56. Wu F-C. Optimization of correlated multiple quality characteristics using desirability function. *Qual Eng*. 2004;17(1):119-126.

How to cite this article: Ayodele BV, Mustapa SI, Mohd Yassin MYB, Abdullah S. Experimental and optimization studies of hydrogen production by steam methane reforming over lanthanum strontium cobalt ferrite supported Ni catalyst. *Int J Energy Res*. 2019;43:8118–8135. https://doi.org/10.1002/er.4808